Simulated Transient Electromagnetic Response for the Inspection of GFRP-Wrapped Concrete Cylinders Using Radar NDE

Tzu-Yang Yu [a] , Burak Boyaci [a] & H. Felix Wu [b]

[a] Civil and Environmental Engineering, University of Massachusetts Lowell , Lowell , Massachusetts , USA

[b] The University of North Texas , Denton , Texas , USA
Accepted author version posted online: 16 Jul 2013.Published online: 30 Jul 2013.

PLEASE SCROLL DOWN FOR ARTICLE

Taylor & Francis
Taylor & Francis Group

SIMULATED TRANSIENT ELECTROMAGNETIC RESPONSE FOR THE INSPECTION OF GFRP-WRAPPED CONCRETE CYLINDERS USING RADAR NDE

Tzu-Yang Yu,[1] Burak Boyaci,[1] and H. Felix Wu[2]

[1]Civil and Environmental Engineering, University of Massachusetts Lowell, Lowell, Massachusetts, USA
[2]The University of North Texas, Denton, Texas, USA

Assessing the subsurface condition of glass fiber reinforced polymer (GFRP)-retrofitted concrete structures is an important inspection problem for the maintenance of reinforced concrete structures retrofitted with high performance composites like GFRP. The objective of this paper is to investigate the radar response of GFRP-concrete cylinders through a parametric study, using the finite difference time domain (FDTD) method. Intact and artificially damaged GFRP-wrapped concrete cylinders were modeled in a two dimensional domain. Considered parameters include the thickness of GFRP wrap/layer, width and depth of artificial defects, and the incident frequency. Modulated Gaussian signals with a carrier frequency ranging from 8 GHz to 18 GHz were used as the incident wave. Field and power responses in both time and frequency domains were investigated. A nonlinear effect due to the variation of defect dimensions is found in both time and frequency responses, indicating the multiple, interlayer scattering effect in the system.

Keywords: finite difference time domain, GFRP-concrete, parametric study, radar/microwave NDE, transient electromagnetic response

1. INTRODUCTION

Rehabilitation using fiber-reinforced polymer (FRP) composites has become a popular option for prolonging the service life of civil infrastructures. Traditional materials such as steel found their own disadvantages, including low strength-to-weight ratio, high construction cost, and low corrosion resistivity, when compared with FRP composites for strengthening purpose. For these reasons, the use of FRP composites for strengthening and repairing reinforced concrete (RC) structures is found in a large number of construction projects and a wide variety of worldwide applications [1–5]. FRP composites used in civil engineering include aramid FRP, carbon FRP, and glass FRP. Glass FRP (GFRP) composites have been adopted since the 1990s [6–11], particularly in the retrofitting of RC elements, such as bridge piers/girders and building columns/beams. Among existing strengthening techniques,

the externally-bonded construction scheme appears to be superior over other schemes for RC structures, mainly due to its effectiveness and efficiency on restoring structural integrity. The trade-off is the loss of surface visibility of concrete cracking since FRP composites are opaque. Such material feature creates an inspection problem in the condition assessment of FRP-retrofitted RC structures.

In order to solve this problem, other nondestructive evaluation (NDE) techniques for FRP-retrofitted RC structures have been developed and applied in laboratory and in practice, including acoustic emission [12,13], ultrasonic [14–16], infrared thermography [17,18], X-ray [19], and radar (microwave) [20–22] techniques. Among these NDE techniques, radar NDE is less vulnerable to environmental disturbances such as temperature and light intensity. Until now, radar NDE has demonstrated its capability for the condition assessment of FRP-retrofitted RC structures, especially for GFRP-RC structures. At the present time, most reported radar NDE techniques for FRP-wrapped concrete structures adopt the contact or near-field inspection scheme [22] which can be expensive (e.g., instrumentation, auxiliary equipment needed, traffic control) and challenging when the accessibility of structures becomes an issue. Near-field radar NDE, sometimes, can also be infeasible when applied to cross-river or cross-valley bridges and highway bridges. On the other hand, far-field radar NDE avoids these difficulties and, thus, is more applicable for practical application. The main difference between near-field and far-field radar NDE is the waveform of radar signals. Near-field radar uses circular/spherical waves and far-field radar uses near-planar or plane waves.

Radar NDE (for both near-field and far-field) involves the generation and transmission of electromagnetic (EM) waves using antennas, specific data collection mode (relative movement between the antenna and the structure), signal processing/imaging algorithms, and a data interpretation strategy. Materials with different dielectric properties can be identified by radar NDE and interpreted by the variation in transmission and reflection coefficients. Based on this principle, voids, delaminations, rebars, and characteristics of matrix materials (e.g., concrete) can be detected/identified. It is also known that EM waves cannot penetrate through metallic media and will attenuate in conductive/lossy dielectrics. Therefore, optimization between the penetration depth and detection capability for civil infrastructures is important. For example, in geotechnical applications (e.g., ground penetrating radar), low frequency EM waves (0.05–1.5 GHz) are usually adopted to achieve better exploration depth, in exchange of sacrificed detectability. In general, with proper development of wideband, multifrequency capability, tomographic imaging techniques and the measurement of dielectric properties, radar NDE can be a powerful tool in assessing structural members made of multiple materials, such as GFRP-wrapped concrete structures.

To better utilize radar NDE for civil infrastructures, their EM response needs to be systematically studied. The purpose of this article is to investigate the transient EM response of GFRP-wrapped concrete structures through a

parametric study by numerical simulation for the better use of radar NDE in civil engineering. Focus is limited to laboratory concrete cylinders corresponding to bridge piers of circular cross section. In this article, intact and damaged GFRP-wrapped concrete cylinders are both considered. Damaged GFRP-wrapped concrete cylinders are simulated by introducing rectangular artificial anomaly (filled by air) at the interface between GFRP layer and concrete core. This artificial defect is characterized by its width and depth, as shown in Fig. 1. In this scenario, other possible structural damages that can occur to real GFRP-wrapped concrete cylinders are simulated by different aspect ratios (width vs. depth) of the defect. High aspect ratios represent the delamination between GFRP and concrete, while low aspect ratios correspond to in-depth concrete cracking (in an idealistic manner). Considered parameters are the thickness of GFRP layer, width and depth of the artificial defect, and incident frequency. Only two-dimensional GFRP-wrapped concrete cylinders were considered, in which the cylinder has an infinite length in the longitudinal direction and a finite cross-sectional area. The reason of choosing two-dimensional structure is to simplify the problem and to amplify the effect of each parameter in the transient EM response of target structure. Numerical simulation of three-dimensional GFRP-wrapped concrete cylinders is ongoing, and results will be reported in the future, along with corresponding experimental measurements.

In the following parts of this article, numerical simulation methodology including Maxwell's curl equations and finite difference time domain (FDTD) methods are provided. Geometrical configuration of the two-dimensional GFRP-wrapped concrete cylinder is described, as well as the dielectric properties of materials used in the simulation. Absorbing boundary conditions (ABC) for modeling open space (infinite domain), spatial and temporal
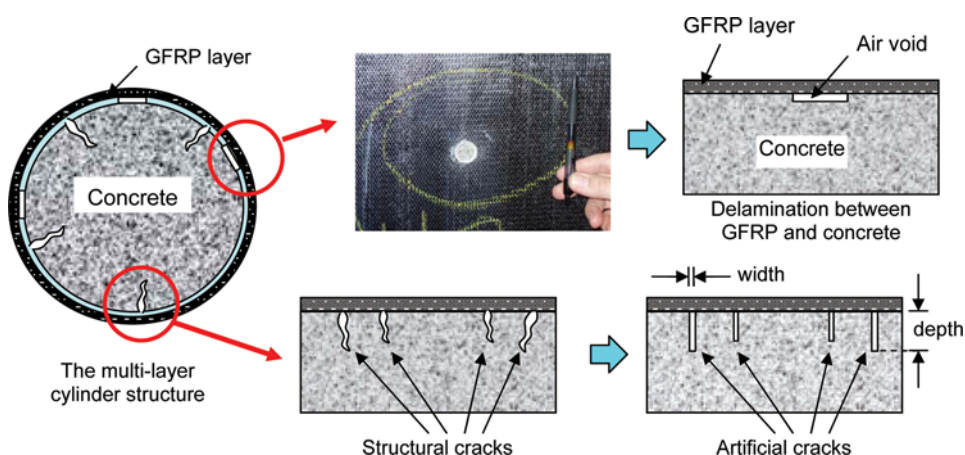

FIGURE 1. Modeling of subsurface damages. (Figure appears in color online.)

discretization criteria, initial conditions, and the configuration of computational domain are also explained. Reflection responses of intact and damaged GFRP-wrapped concrete cylinders are investigated in both time and frequency domains. Time delay of arrival and maximum amplitude in time domain response, as well as the change in frequency spectrum, are applied to study the effects of considered parameters. Finally, conclusions drawn from this simulation work are reported and discussed.

2. RESEARCH METHODOLOGY

2.1. Maxwell's Curl Equations

Radar signals or microwaves are governed by the laws of electricity and magnetism which can be described by Maxwell's equations. For the purpose of numerical implementation using difference equations, the curl form of Maxwell's equations is adopted. In linear and isotropic media, Maxwell's curl equations for source-free problems are read [23]:

$$\nabla \times \overline{H} = \frac{\partial}{\partial t}\overline{D} \tag{1}$$

$$\nabla \times \overline{E} = -\frac{\partial}{\partial t}\overline{B} \tag{2}$$

$$\nabla \cdot \overline{D} = 0 \tag{3}$$

$$\nabla \cdot \overline{B} = 0 \tag{4}$$

where $\overline{H}$ = magnetic field strength (amperes/m or A/m), $\overline{D}$ = electric displacement (coulombs/m^2 or C/m^2), $\overline{E}$ = electric field strength (Volts/m or V/m), and $\overline{B}$ = magnetic flux density (webers/m^2). These quantities are real functions of position and time. The constitutive relations of EM waves in dielectrics are

$$\overline{D} = \varepsilon\overline{E} = \varepsilon_0\varepsilon_r\overline{E} \tag{5}$$

$$\overline{B} = \mu\overline{H} = \mu_0\mu_r\overline{H} \tag{6}$$

where ε = electric permittivity of the medium (farads/m or F/m), $\varepsilon_0 = 8.8542 \times 10^{-12}$ F/m = permittivity of free space, ε_r = relative permittivity, μ = magnetic permeability of the medium (henrys/m or H/m), $\mu_0 = 4\pi \times 10^{-7}$ H/m = permeability of free space, μ_r = relative permeability. After substituting Eqs.(5) and (6) into Eqs. (1) and (2), only six unknowns (e.g., in Cartesian coordinate systems, E_x, E_y, E_z, H_x, H_y, and H_z) are to be found. Since Eqs. (1) and (2) provide six scalar equations at the component level, the six unknowns can be

fully determined. Rearranging the components in Eqs. (1) and (2) leads to two decoupled groups of governing equations which can be evaluated independently with each other. Considering x-y as the plane of incidence, the group containing H_x, H_y, and E_z is called transverse magnetic (TM) mode. The other group containing E_x, E_y, and H_z is called transverse electric (TE) mode. EM waves operating in TE and TM modes are termed TE and TM waves, respectively. In this paper, no perfect conductor is considered in the simulation, suggesting that TE wave and TM wave simulations can be converted by the principle of duality. Details of the principle of duality can be found in Kong [23]. In all simulation cases, TE waves were used.

In two-dimensional problems in which x-y plane constitutes the plane of incidence, EM fields are constant in z-axis, and thus, $\partial/\partial z = 0$. The component representation of TE waves in Cartesian coordinate systems has three equations as follows:

$$\frac{\partial E_x}{\partial t} = \frac{1}{\varepsilon}\left(\frac{\partial H_z}{\partial y}\right) \tag{7a}$$

$$\frac{\partial E_y}{\partial t} = -\frac{1}{\varepsilon}\left(\frac{\partial H_z}{\partial x}\right) \tag{7b}$$

$$\frac{\partial H_z}{\partial t} = -\frac{1}{\mu}\left(\frac{\partial E_y}{\partial x} - \frac{\partial E_x}{\partial y}\right). \tag{7c}$$

Taking the partial derivatives of Eqs. (7a) and (7b) with respect to time and substituting them into Eq. (7c) provides

$$\left(\frac{\partial^2}{\partial x^2} + \frac{\partial^2}{\partial y^2} - \mu\varepsilon\frac{\partial^2}{\partial t^2}\right)H_z = 0. \tag{8}$$

Equation (8) is the Helmholtz wave equation for TE waves. E_x and E_y can be found once H_z is determined theoretically by given boundary conditions.

2.2. Finite Difference Time Domain Methods

Maxwell's curl equations are evaluated by finite difference methods in both space and time domains. Discretization is based on Yee's algorithm in which E_x, E_y, and H_z are solved in an interleaving scheme [24]. Yee's algorithm uses central difference scheme with second-order accuracy for evaluating EM field quantities. Explicit solution to Maxwell's curl equations can be obtained for direct numerical implementation.

The FDTD method using Yee's algorithm was implemented by a two-dimensional code written in Matlab (Matrix Laboratory®), developed by the authors. This code is written for studying two-dimensional EM scattering

problems and capable of simulating TE and TM waves. Details of numerical simulation such as discretization criteria, boundary conditions, initial conditions, and the configuration of computational domain are described in the following sections.

In Yee's definition, the time and space dependent EM field quantities are denoted. Take E_x as an example:

$$E_x(x, y, z, t) = E_x(i\Delta x, j\Delta y, k\Delta z, n\Delta t) = E_x|_{i,j,k}^n \qquad (9)$$

where (x, y, z) = spatial coordinate, t = temporal coordinate, (i, j, k) = subscripts in (x, y, z), $(\Delta x, \Delta y, \Delta z)$ = spatial increment, and Δt = temporal increment. For two-dimensional problems, variations of EM field quantities in the z-axis diminish. Following Yee's definition, the Taylor series expansions of $E_x|_{i+1,j,k}^n$ and $E_x|_{i-1,j,k}^n$ are

$$E_x|_{i+1,j,k}^n = E_x|_{i,j,k}^n + \Delta x \cdot \frac{\partial E_x}{\partial x}\Big|_{i,j,k}^n + \frac{(\Delta x)^2}{2} \cdot \frac{\partial^2 E_x}{\partial x^2}\Big|_{i,j,k}^n + \frac{(\Delta x)^2}{6} \cdot \frac{\partial^3 E_x}{\partial x^3}\Big|_{i,j,k}^n + \cdots$$

$$(10a)$$

$$E_x|_{i-1,j,k}^n = E_x|_{i,j,k}^n - \Delta x \cdot \frac{\partial E_x}{\partial x}\Big|_{i,j,k}^n + \frac{(\Delta x)^2}{2} \cdot \frac{\partial^2 E_x}{\partial x^2}\Big|_{i,j,k}^n - \frac{(\Delta x)^2}{6} \cdot \frac{\partial^3 E_x}{\partial x^3}\Big|_{i,j,k}^n + \cdots$$

$$(10b)$$

$\frac{\partial E_x}{\partial x}\big|_{i,j,k}^n$ and $\frac{\partial^2 E_x}{\partial x^2}\big|_{i,j,k}^n$ can be obtained by adding and subtracting Eqs. (10a) and (10b). Similar treatment also applies to $\frac{\partial E_x}{\partial t}\big|_{i,j,k}^n$ and $\frac{\partial^2 E_x}{\partial t^2}\big|_{i,j,k}^n$. In Yee's algorithm, $\Delta x/2$ was used instead of Δx. $\overline{E}$ components are evaluated at intervals of Δx and Δt, while $\overline{H}$ components are at intervals of $\Delta x/2$ and $\Delta t/2$. The same discretization scheme is adopted in the numerical study of this manuscript. In other words, they are interleaved in space and time domains. Figure 2 shows the positions of EM field quantities in Yee's cubic cell lattice. The interleaving time-stepping process is illustrated in Fig. 3 using the x-y plane as an example. Positive directions of EM field quantities are also indicated in Fig. 3. With Yee's discretization scheme, the second-order accurate finite difference approximation of Eq. (7a) becomes

$$\frac{E_x|_{i+1/2,j+1,k}^n}{\Delta t} = \frac{E_x|_{i+1/2,j+1,k}^{n+1/2} - E_x|_{i+1/2,j+1,k}^{n-1/2}}{2\Delta t}$$
$$= \left(\frac{1}{\varepsilon_{i+1/2,j+1,k}}\right)\left[\frac{H_z|_{i+1/2,j+1,k+1/2}^n - H_z|_{i+1/2,j+1,k-1/2}^n}{\Delta y}\right] \qquad (11)$$

FIGURE 2. Positions of EM field quantities in Yee's cubic cell lattice for transverse electric waves.

or

$$E_x\big|_{i+1/2,j+1,k}^{n+1/2} = E_x\big|_{i+1/2,j+1,k}^{n-1/2}$$
$$+ \left(\frac{\Delta t}{\varepsilon_{i+1/2,j+1,k}}\right)\left[\frac{H_z\big|_{i+1/2,j+1,k+1/2}^{n}-H_z\big|_{i+1/2,j+1,k-1/2}^{n}}{(\Delta y/2)}\right]. \quad (12)$$

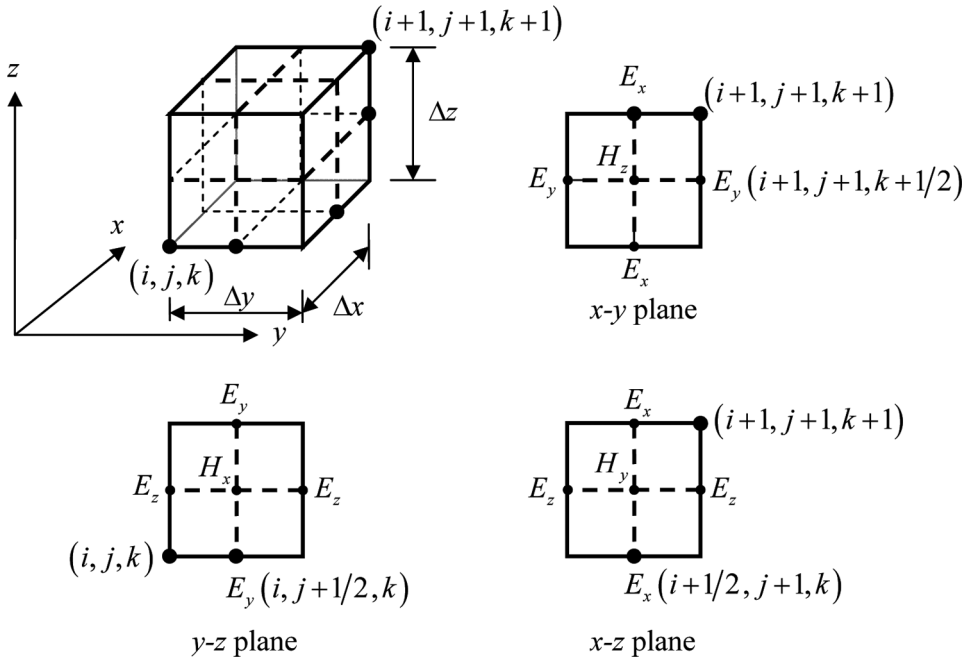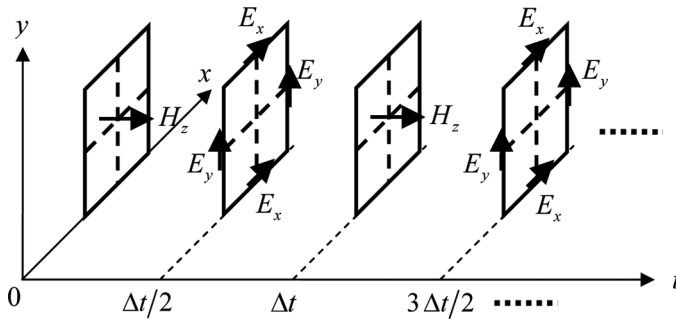**FIGURE 3.** Space-time representation of the time-stepping process for transverse electric waves.

The finite difference approximations of Eqs. (7b) and (7c) can also be derived by the same approach. EM field quantities in time step $(n + 1)$ are fully determined by previous values. In source-free problems, self-equilibrium among EM field quantities is achieved when time-dependent initial conditions are provided. For TE waves H_z is used for introducing initial conditions and E_z for TM waves.

2.3. Discretization Criteria and Boundary Condition

The selection of temporal and spatial increments must satisfy both the sampling criterion and the stability criterion. Aliasing errors can occur when undersampling the EM response. To avoid the aliasing error, the maximum sampling rate in time Δt_N (sec) must obey the following criterion, based on the Nyquist (folding) frequency:

$$\Delta t_N < \frac{1}{2f_{max}}, \tag{13}$$

where f_{max} = maximum temporal frequency (Hz) in the response. Similarly, the maximum sampling rate in space Δx_N (m) can also be defined:

$$\Delta x_N < \frac{\pi}{k_{max}} \tag{14}$$

where k_{max} = maximum spatial frequency (or wavenumber) (rad/m).

The Courant–Friedrichs–Lewy (CFL) stability criterion was proposed by [25] for translating partial differential equations into algebraic equations and for solving partial differential equations based on numerical stability. Taflove and Brodwin [26] further derived the maximum time increment Δt_{CFL} for three-dimensional problems

$$\Delta t_{CFL} \leq \frac{1}{c\sqrt{\frac{1}{\Delta x^2} + \frac{1}{\Delta y^2} + \frac{1}{\Delta z^2}}}. \tag{15}$$

Given a uniform discretization scheme ($\Delta x = \Delta y = \Delta z$), Eq. (15) can be rewritten as

$$\Delta t_{CFL} \leq \frac{\Delta x}{c\sqrt{n}} \tag{16}$$

where n is the dimension of the problems. The physical meaning of Eq. (15) is the constraint of causality in numerical computation; the selected time increment must be less than the shortest traveling time for EM waves between any two grid points in a lattice cell. In this paper, Δx was chosen as 0.0015 m and Δt as $\Delta x/(2c) = 0.0025$ ns. Using Eq. (14), this selection corresponds to

a maximum frequency of 100 GHz. The maximum frequency used in this numerical simulation is 18 GHz, and the selection of Δx satisfies the sampling criterion. In the frequency range of 8–18 GHz, the chosen time increment Δt satisfies both the sampling criterion ($1/(2 \times 18 \times 10^9) = 0.0277$ ns) and the CFL criterion ($\Delta t_{CFL} = 0.0035$ ns). In this example, the CFL criterion is stricter than the sampling criterion.

ABC were applied at the borders of the finite, computational domain in order to simulate a physically infinite space. The structure is considered being placed in an open space where reflected waves from other objects do not interfere with the main response from the structure. Simulations in such environment require the use of ABC in the computational domain. The perfectly matched layer (PML) ABC proposed by Berenger [27] was used in this study. The PML is constituted of an absorbing medium whose dielectric properties satisfy the following condition:

$$\frac{\sigma}{\varepsilon_0} = \frac{\sigma^*}{\mu_0} \tag{17}$$

where $\sigma =$ electric conductivity (mho/m or siemens/m or S/m) and $\sigma^* =$ magnetic conductivity (Ohm/m or O/m). This requirement leads to the zero impedance of the absorbing medium, which consequently produces no reflection from the medium upon the impinging of outgoing waves from inside the computational domain. Detailed information about the design of PML ABC can be found in [28, 29].

2.4. Initial Condition and Incident Waves

In this paper, modulated Gaussian waves were used as the input signal for their advantages over other waveforms, mainly due to the ease of frequency modulation. The far-field condition of radar NDE was simulated by the use of plane waves in simulation. Huygens' principle was applied for the introduction of plane wave incidence. For TE waves, modulated Gaussian signals for H_z are in the following form:

$$H_z(\omega_c, t) = H_0 \cdot \sin(\omega_c t) \cdot \exp\left[-\left(\frac{t}{\tau}\right)^2\right] \tag{18}$$

where $H_0 =$ maximum amplitude of $H_z(\omega_c, t)$(A/m), $\omega_c =$ carrier frequency of the signal (rad/s), $t = n_i\Delta t$ (sec), $n_i = n_{istart} \sim n_{iend}$, $n_{length} =$ total length of the signal, $\Delta t =$ time increment (sec), and $\tau =$ duration of the modulated Gaussian (sec). It can be seem that the exponential term modulates the frequency content of the signal. Also,

$$H_z(\omega_c, n_i\Delta t) = \begin{cases} 0 & n_i < n_{istart}, n_i > n_{iend} \\ H_z(\omega_c, t), & n_{istart} \leq n_i \leq n_{iend}. \end{cases} \tag{19}$$

H_z waves of carrier frequencies at 4 GHz and 9 GHz are illustrated in Fig. 4. The Poynting power density $\langle S \rangle$ (W/m^2) was used for evaluating the power response of the cylinder, determined by the equation

$$\langle S \rangle = \frac{1}{2} \text{Re}\{\overline{E} \times \overline{H}^*\} \tag{20}$$

where $\overline{E} = \hat{x}E_x + \hat{y}E_y = \frac{-1}{i\omega\varepsilon}\nabla \times \overline{H}$ (V/m), $\overline{H} = \hat{z}H_z$ (A/m), and $\overline{H}^*$ is the conjugate of $\overline{H}$(A/m). From Eq. (20), it is clear that the carrier frequency of $\langle S \rangle$ is twice the value of the one of H_z. Frequency spectra of $\langle S \rangle$ with carrier frequencies at 8 GHz and 18 GHz are shown in Fig. 5. Incident EM waves (radar signals) were introduced at $x = 50$ grids (0.075 m or 2.95 in) from the left boundary in the computational/rectangular domain. Reflected waves from the GFRP-concrete cylinder were collected at the same location. The carrier frequency of H_z ($f_c = \omega_c/(2\pi)$) ranged from 4 GHz to 9 GHz, while f_c ranged from 8 GHz to 18 GHz for the average Poynting power S.

Description of the Structure   The dimensions of the numerical domain were 800 grids in x-axis and 400 grids in y-axis, virtually simulating a 1.2 m-by-0.6 m physical space (Fig. 6). Uniform discretization in space was applied with $\Delta x = \Delta y = 0.0015$ m (0.059 in) to be the spatial increment in the simulation. Figure 6 shows the configuration of aGFRP-wrapped concrete cylinder in the computational domain. This cylinder was made of a concrete core with a diameter of 0.153 m (6 in) and an externally wrapping GFRP layer of thickness 0.003 m (0.118 in) per layer. The GFRP layer was consisted of GFRP fabric and molded by epoxy (also used as an adhesive for bonding GFRP onto the surface of concrete). Structural damage in the cylinder was simulated by the introduction of an artificial defect at the interface between the concrete and
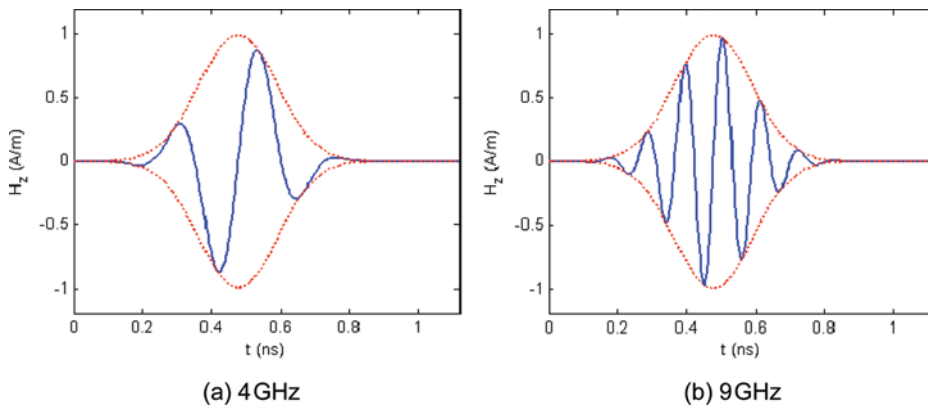

FIGURE 4. H_z waves of carrier frequencies 4 and 9 GHz. (Figure appears in color online.)
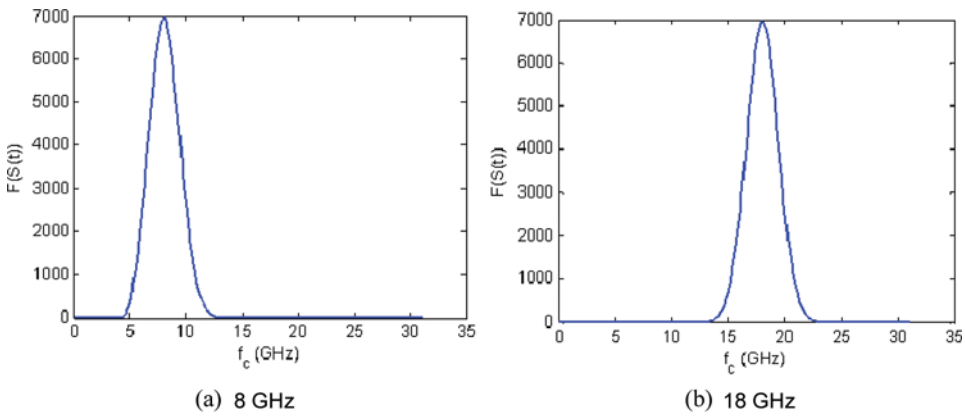
(a) 8 GHz   (b) 18 GHz

FIGURE 5. Frequency spectra of $\langle S \rangle$ with two carrier frequencies. (Figure appears in color online.)

the GFRP layer. Seven types of artificial defects with different depths and widths were considered in this study. An illustration depicting the GFRP-wrapped concrete cylinder is provided in Fig. 7, together with considered parameters. Artificial defects of seven damage scenarios (DS01–DS07) are summarized in Table 1. High depth-to-width ratios (such as DS07) character-ize concrete cracking in the vicinity of GFRP-concrete boundary (in an ideal way), while high width-to-depth ratios(such as DS04) characterize GFRP
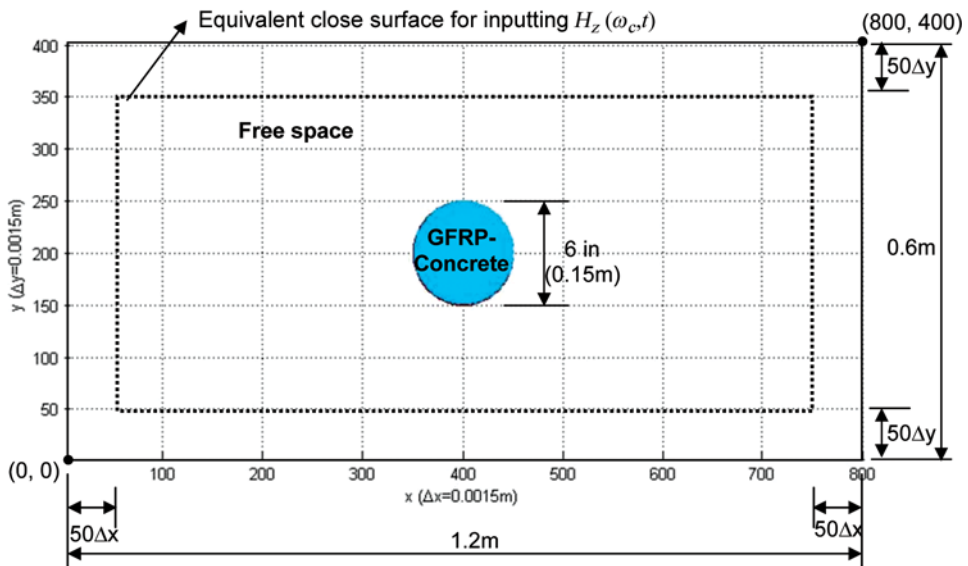
FIGURE 6. Configuration of the GFRP-concrete cylinder and the computational domain. (Figure appears in color online.)

FIGURE 7. GFRP-wrapped concrete cylinder and considered parameters.

TABLE 1 Damage Scenarios

Damage scenario	Illustration	Depth (in)	Width (in)	Damage scenario	Illustration	Depth (in)	Width (in)
DS01		1	1	DS05		1	1/2
DS02		1/2	1	DS06		1	1/4
DS03		1/4	1	DS07		1	1/8
DS04		1/8	1				

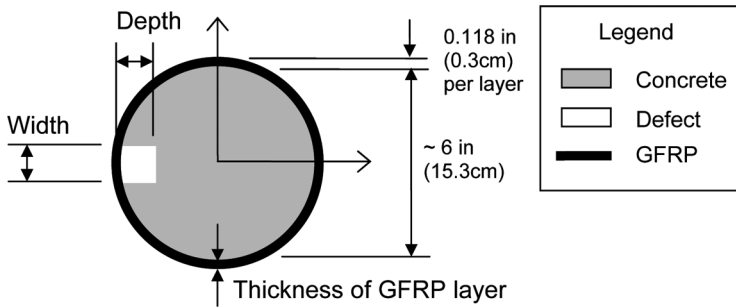**TABLE 2** Dielectric Properties of Materials

Material	Dielectric constant, ε'_r	Electrical conductivity σ (S/m)	Relative magnetic permeability, μ'_r
Air	1	0	1
Dry concrete	5	0.05	1
GFRP	4	0.01	1

delamination, both simulating structural damages in real GFRP-retrofitted concrete columns.

Dielectric Properties of Materials The dielectric constant of hardened Portland cement concrete generally varies from 5 (dry concrete) to 25 (wet concrete), depending on moisture content, material composition (e.g., water-to-cement ratio), measurement temperature, and measurement frequency. Among these factors, moisture content plays a critical role in increasing the dielectric constant and electrical conductivity of concrete. Wet concrete exhibits a dispersive (frequency-dependent) behavior in its dielectric properties, while dry concrete shows a low-dispersive or nondispersive behavior in some microwave frequency ranges. Beside the inherent dielectric properties of solid components in concrete, the amount and the distribution of free ions carried by moisture residing inthe capillary pores in concrete also affect the dielectric polarizibility and electrical conductivity of concrete. In dry concrete, the lack of linkage among these ions changes its polarization upon the application of EM fields, as well as the ability it conducts electric current. In the frequency range of 8–18 GHz, the dielectric properties of dry concrete were reported as almost constant [30]. In this simulation work, the dielectric constant and electrical conductivity of concrete are assumed to be constant, corresponding to the case of dry concrete in reality.

The dielectric properties of GFRP were ε'_r (dielectric constant) $= 3–5$ and σ (electrical conductivity) $= 0.005–0.03$ S/m, representing E-glass FRP. Since in the frequency range 8–18 GHz, variations of ε'_r and σ of GFRP are insignificant and the thickness of GFRP layer is very thin, ε'_r and σ of GFRP are taken to be constant in the simulation ($\varepsilon'_r = 4$ and $\sigma = 0.01$ S/m). Dielectric properties of materials used in this article are summarized in Table 2.

3. SIMULATION RESULTS

In the response of a layered dielectric medium subjected to transient EM waves, multiple reflections and scattering of EM waves can occur. In this study, the arrival time of reflected waves was estimated in order to determine the duration of simulation. Transient response analysis of the GFRP-concrete cylinder was performed by studying the first reflection from the back of the cylinder (Fig. 8). This reflection signal contains characteristics of the GFRP-concrete
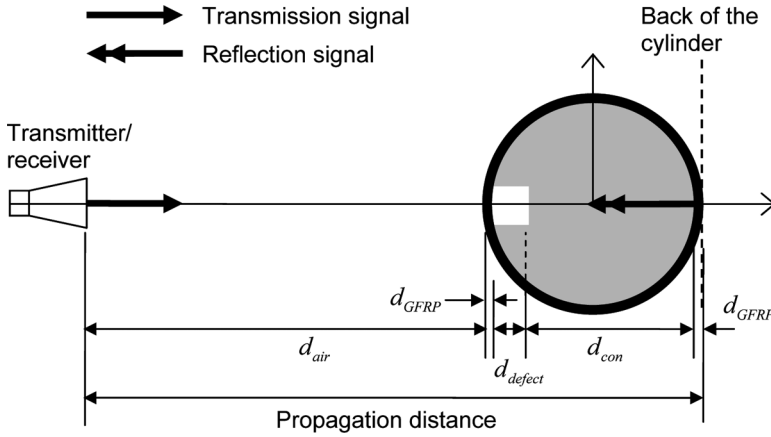
FIGURE 8. First reflection from the back of the cylinder.

cylinder because it travels through the entire cylinder, including the artificial defect. Identification of the first reflection signal in the time-domain response was achieved by calculating the arrival time of the signal. The arrival time of reflection signal can be precisely computed with the information of structure configuration and material properties. The peak-to-peak time was used for determining the departure and arrival moments of EM waves in the response. Total propagation time of the first reflection signal was the time EM waves traveling twice the propagation distance (shown in Fig. 8), determined by

$$t_{total} = 2\left(\frac{d_{air} + d_{defect}}{c} + 2 \cdot \frac{d_{GFRP}}{v_p|_{GFRP}} + \frac{d_{con}}{v_p|_{con}}\right) \qquad (21)$$

where t_{total} = total traveling time (sec), d_{air}, d_{GFRP}, d_{defect}, and d_{con} = traveling distances in free-space, GFRP layer, artificial defect, and concrete (all in meters), respectively. $c = 2.9979 \times 10^8$ m/s = EM wave velocity in free space, $v_p|_{GFRP}$ and $v_p|_{con}$ = EM wave phase velocities in GFRP and concrete (m/s). The phase velocity of EM waves in lossy (conductive) media is determined by [23]

$$v_p = \frac{\omega}{k_R} = \frac{1}{\sqrt{\mu\varepsilon}} \cdot \left[\frac{1}{2}\left(\sqrt{1 + \left(\frac{\sigma}{\omega\varepsilon}\right)^2} + 1\right)\right]^{-1/2}$$

$$= \frac{c}{\sqrt{\mu_r'\varepsilon_r'}} \cdot \left[\frac{1}{2}\left(\sqrt{1 + \left(\frac{\sigma}{\omega\varepsilon}\right)^2} + 1\right)\right]^{-1/2} \qquad (22)$$

where ω = angular frequency (rad/sec), k_R = real part of the complex wave number (rad/m), $k = k_R + j \cdot k_I$ (rad/m), μ = magnetic permeability (H/m),

$\varepsilon =$ electric permittivity (F/m), $\sigma =$ electrical conductivity (S/m), $\mu'_r =$ relative permeability, and $\varepsilon'_r =$ relative permittivity (dielectric constant). Calculated phase velocities of EM waves in three considered media are summarized in Table 3. The phase velocity of EM waves in GFRP (1.499×10^8 m/s) is faster than the one in dry concrete (1.341×10^8 m/s), as shown in Fig. 9. With the phase velocities in the materials and the damage scenarios in Table 1, total traveling times for intact and DS01–DS07 cylinders were calculated (listed in Table 4). The minimum run time of simulation is the summation of total traveling time and signal length. It must be long enough to capture the entire reflection waveform, while remaining as short as possible for the sake of computational efficiency. Signal length was designed to be $250\,\Delta t$ in the simulation, and the used runtime was $2{,}500\,\Delta t$, which is sufficient to include the entire reflection waveform.

The transient response of reflected waves was collected from cylinders with various integrity configurations (intact, DS01–DS07). Multiple reflections were also generated from this stratified structure, but only the target reflection was used. The frequency spectrum of incident waves is produced by the Fast Fourier Transform (FFT) and represented in power density (W/m^2) and decibel (dB), as shown in Fig. 10. The spectrum of reflected waves from the 1-layer GFRP intact cylinder is shown in Fig. 11. Low frequency contents (below 5 GHz) in the spectrum were not used for analysis since the characteristic length of the artificial defect falls in the frequency range of 8 GHz to 12 GHz (wavelength $= 0.0375$–0.025 m or 1.47–0.98 in).

Comparison between Figs. 10 and 11 indicates that the frequency content of incident waves is changed only for some frequencies. The presence of concrete cylinder (without GFRP) introduces ripples in the vicinity of main lobe (dashed line) in the spectrum. On the other hand, the shape of main lobe in the reflection spectrum is basically preserved.

3.1. Effects of GFRP Thickness

The presence of GFRP layer in the concrete cylinder is expected to introduce extra time delay and amplitude attenuation in reflected waves when

TABLE 3 Phase Velocities in Various Media

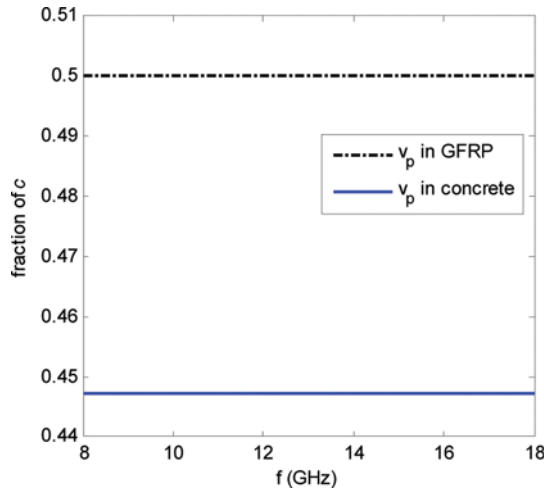| Medium	ε'_r	σ (S/m)	Phase velocity v_p (m/s)
Air	1	0	C
Concrete (dry)	5	0.05	$\dfrac{c}{\sqrt{5}} \cdot \left[\dfrac{1}{2} \left(\sqrt{1 + \left(\dfrac{0.18}{f}\right)^2} + 1 \right) \right]^{-1/2}$, where f is the freq. in GHz
GFRP	4	0.01	$\dfrac{c}{2} \cdot \left[\dfrac{1}{2} \left(\sqrt{1 + \left(\dfrac{0.045}{f}\right)^2} + 1 \right) \right]^{-1/2}$

FIGURE 9. Phase velocities of EM waves in dry concrete and GFRP. (Figure appears in color online.)

compared to the response from the concrete cylinder without GFRP. The electric permittivity of GFRP delays the speed of EM waves, and the conductivity also consumes the energy of EM waves. Four GFRP configurations (no GFRP, 1-layer, 2-layer, and 3-layer) with different GFRP thicknesses for intact and artificially damaged cylinders were investigated. Target reflected waves were collected and analyzed to study the effect of GFRP thickness in the time delay of arrival, maximum amplitude, and frequency variation.

The time delay was calculated by extracting the time difference between the reflection responses of cylinders with and without GFRP. For the intact cylinder, a two-dimensional stratified plate model was used for demonstrating the effect, as shown in Fig. 12(b). In Fig. 12(b), the plate model consists of GFRP and concrete with same thicknesses. The theoretical time delay Δt_{plate} in the plate model is calculated by

$$\Delta t_{plate} = 2 \left(2 \frac{d_{GFRP}}{v_p \big|_{GFRP}} - \frac{d_{GFRP}}{c} \right) \tag{23}$$

TABLE 4 Total Traveling Time for the First Reflection

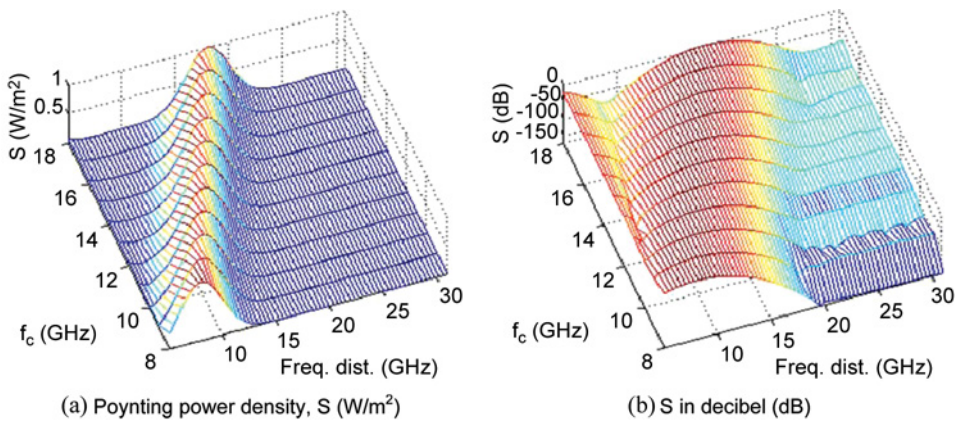| Structural type	Traveling time (ns)	Time step (Δt)
1-layer GFRP, intact	5.334499	2132
1-layer GFRP, DS01	5.136588	2053
1-layer GFRP, DS02	5.235544	2093
1-layer GFRP, DS03	5.285021	2113
1-layer GFRP, DS04	5.309760	2122
1-layer GFRP, DS05 $\sim$ 07	5.136588	2053

FIGURE 10. Frequency spectrum of incident waves. (Figure appears in color online.)

where $v_p|_{GFRP}$ is the phase velocity of EM waves in GFRP (m/s). Results of Eq. (23) for various GFRP configurations are denoted by the dashed line in Fig. 13, where the time delay is represented in terms of time increment Δt.

In Fig. 13, proportionality is found in the result of the plate model. The FDTD solution of the GFRP-concrete cylinder (denoted by the solid line in Fig. 13) deviates from the straight-line result of the plate model but generally exhibits proportionality with the presence of GFRP (1-layer). The FDTD solution of the difference in the 1-layer GFRP-concrete cylinder model is close to the theoretical calculation of the difference in the 1-layer GFRP-concrete plate model. The deviation of two lines in Fig. 13 is attributed to the difference in target's geometry. Such difference is amplified by increasing the
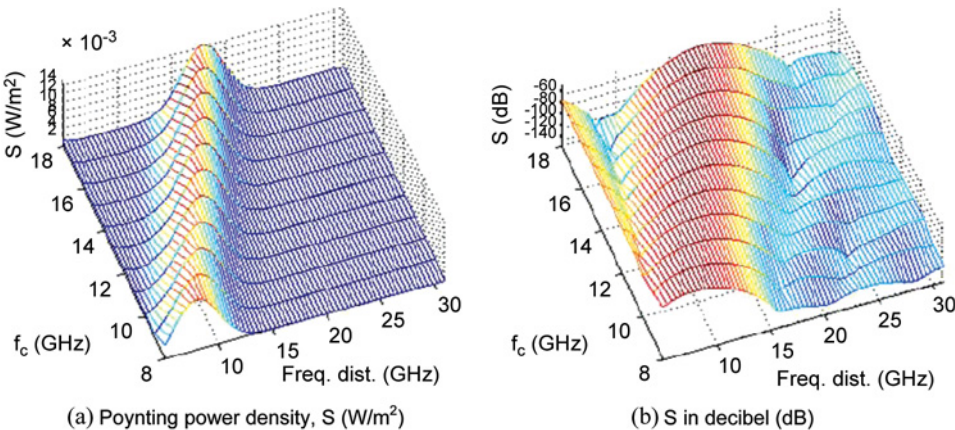

FIGURE 11. Frequency spectrum of reflected waves from the concrete cylinder without GFRP. (Figure appears in color online.)

(a) 1-layer GFRP-concrete cylinder model   (b) 1-layer GFRP-concrete plate model
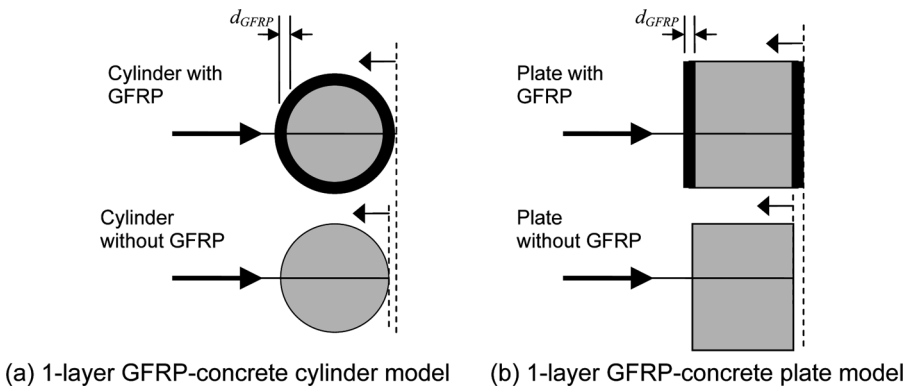
FIGURE 12. GFRP-concrete cylinder and the plate model.

thickness of GFRP. As shown in Fig. 13, the thicker the GFRP layer, the more difference between the plate model and the cylinder. The increase of GFRP thickness also encourages the scattering effect in this stratified structure.

Meanwhile, the maximum amplitude of reflected waves is influenced by the dielectric properties (loss factor or conductivity) of materials and wave scattering. Unlike the reflection response of stratified planar structures upon the impinging of plane waves, creeping waves can occur on the circular surface of cylinders. The creeping waves propagating within the GFRP layer travels faster than the transmitting wave in the concrete cylinder. On the
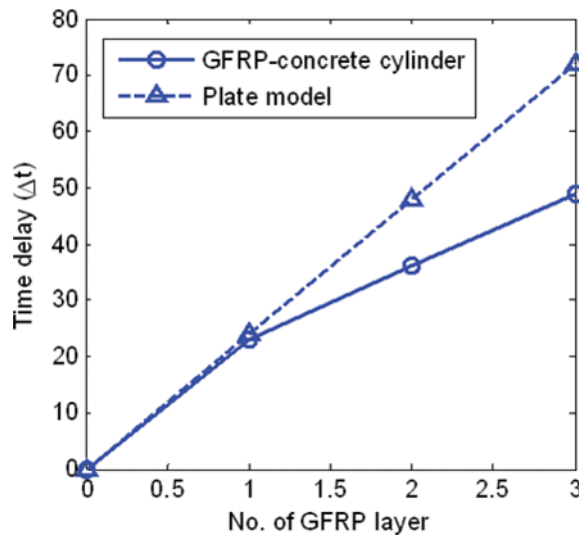

FIGURE 13. Time delay of arrival vs. the number of GFRP layer. (Figure appears in color online.)

other hand, the effect due to the presence of creeping waves in the maximum amplitude of reflected waves is counteracted by the longer distance it takes to reach the reflection line (Fig. 12) from the transmitter antenna. Additionally, creeping waves affect the maximum amplitude by changing the waveform of reflected waves.

Numerical simulations of concrete cylinders with various GFRP configurations were carried out to investigate the influence of GFRP thickness on maximum amplitude. As the combined result of the factors mentioned above, the maximum amplitude of reflected waves not only varies with the GFRP thickness, but also with the measurement frequency. Figures 14(a) and (b) show simulation results from the intact concrete cylinder and the DS01 cylinder at various GFRP thicknesses. Generally, the amplitude of reflected waves from the cylinder without GFRP is greater than those with GFRP. In Figs. 14(a) and (b) at frequencies where the curves intersect, a change of waveform was observed. For example, the incident wave at center frequency of 8 GHz produces the reflected wave from the intact cylinder as shown in Fig. 15(a). While the second peak is greater than the first one at 8 GHz, the maximum amplitude shifts to another peak at 12 GHz. In brief, this peak-shifting behavior occurs at the frequencies where the curves intersect in Fig. 14. A similar phenomenon was also found in the response of artificially damaged cylinders, such as the DS01 cylinder (Fig. 14(b)).

Changes in frequency content between the response of cylinders with and without GFRP layer were evaluated using the time-average Poynting power density spectrum. In Fig. 16, aside-lobe (dark dashed line) developing along with the main lobe (white dashed line) was observed on intact cylinders (with and without GFRP layer). This side-lobe becomes less distinguishable when the thickness of GFRP increases, as shown in Fig. 16.
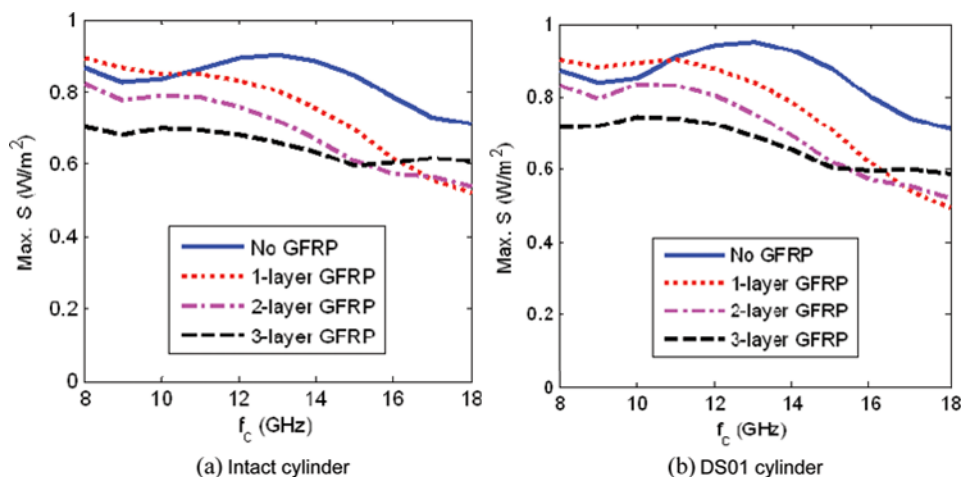

FIGURE 14. Maximum amplitude of reflected waves. (Figure appears in color online.)
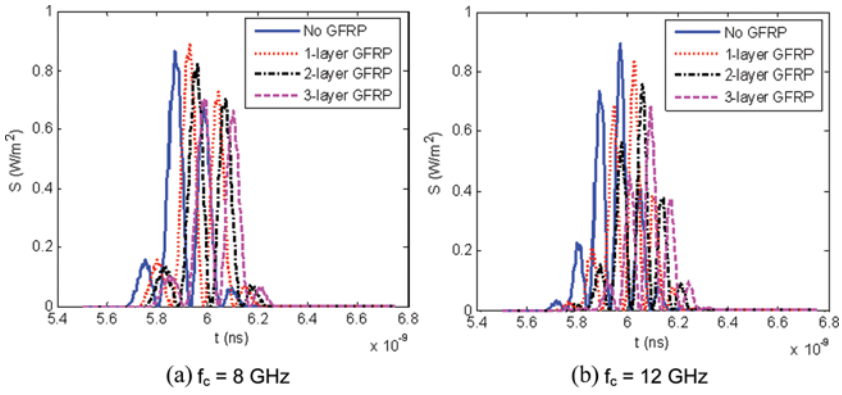
(a) f_c = 8 GHz (b) f_c = 12 GHz

FIGURE 15. Maximum amplitude of reflected waves. (Figure appears in color online.)

(a) Concrete cylinder without GFRP (b) Concrete cylinder with 1-layer GFRP

(c) Concrete cylinder without 2-layer GFRP (d) Concrete cylinder with 3-layer GFRP
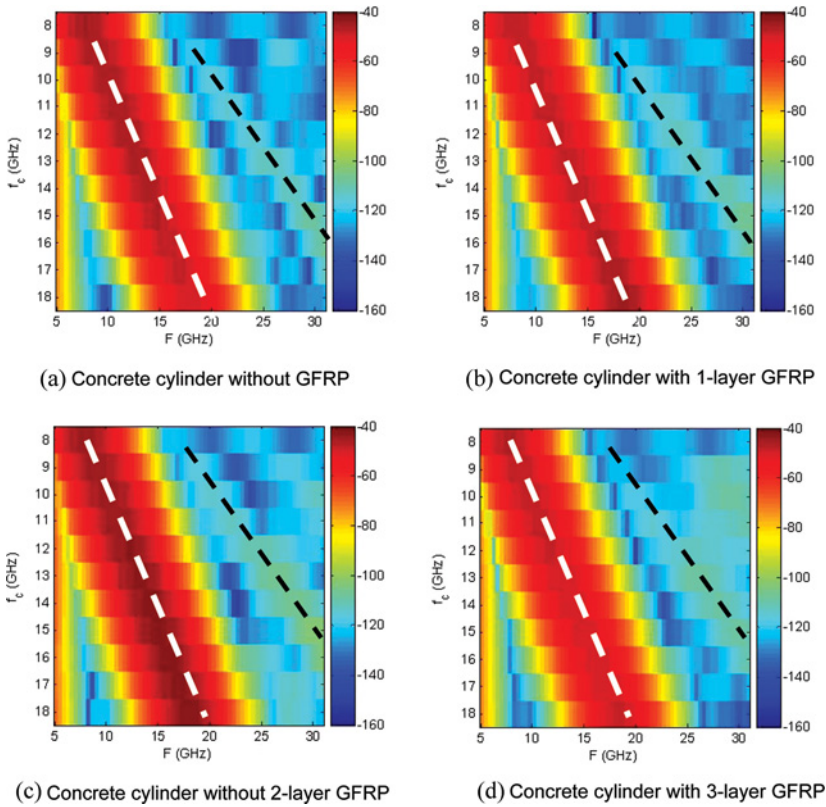
FIGURE 16. Spectrum of reflected waves from cylinders with and without GFRP layer. (Figure appears in color online.)

3.2. Effects of Defect Depth

The effect of artificial defect depth in the reflection response of GFRP-concrete cylinders was studied by comparing the responses of DS04 (depth = 0.3175 cm or 1/8 in), DS03 (depth = 0.635 cm or 1/4 in), DS02 (depth = 1.27 cm or 1/2 in), and DS01 (depth = 2.54 cm or 1 in) cylinders (Table 1) with 1-layer GFRP wrapping. For these cylinders, the width of artificial defect was kept constant as 2.54 cm (1 in). Figure17 shows the amplitude of maximum reflection power response with respect to various defect depths and frequencies. The damaged cylinder with 2.54 cm (1 in) depth defect generates stronger reflection response than the cylinders with defect of 1.27 cm (1/2 in), 0.635 cm (1/4 in), 0.3175 cm (1/8 in), and 0 cm depths (Fig. 17(b)). This difference is more significant in a lower frequency range (8–14 GHz). Similar findings were observed in the comparison among cylinders without GFRP, with 2-layer GFRP, and with 3-layer GFRP.

Using the response of an intact cylinder as the baseline to calculate the damaged responses deviating from the baseline leads to Fig. 18. In Fig. 18, the defect depth is denoted by the fraction of maximum depth. For cylinders without GFRP wrapping (Fig. 18(a)), proportionality is found between the difference in power response and the depth of artificial defect in the frequency range of 11–12 GHz. This frequency range corresponds to wavelengths 2.7–2.5 cm (0.98–1.07 in) in which the defect width (2.54 cm or 1 in) resides. The defect width can be considered as an entrance for the incidence of EM waves to enter the defect. For cylinders with same defect width, their input EM energy is identical. Wave attenuation is proportional to the space occupied by concrete in the direction of wave propagation, which relates to the defect depth. This explanation is further illustrated by a simplified model
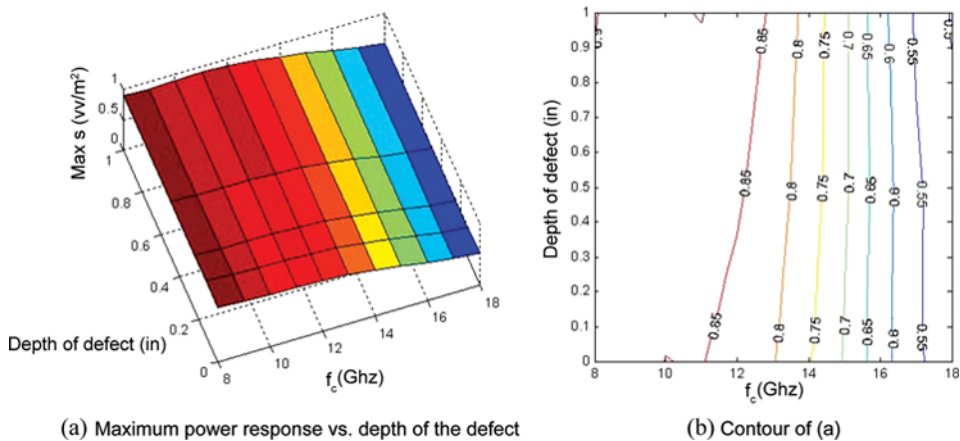

(a) Maximum power response vs. depth of the defect   (b) Contour of (a)

FIGURE 17. Maximum power response of damaged cylinders with various defect depths. (Figure appears in color online.)

shown in Fig. 19. The proportionality between defect depth and wave amplitude difference is observed, while wave scattering due to the geometrical configuration of the cylinder also plays a role in the response.

This proportionality property is further affected by the presence of GFRP layer. For cylinders with GFRP wrapping, proportionality only holds for defects with depth greater than $0.635\,cm$ ($1/4\,in$) in the cases considered in this simulation work. Generally speaking, the increase of GFRP thickness has negative influence on the maximum amplitude of reflected waves, while it also enhances the proportionality between power difference (ΔS) and the defect depth. In Fig. 20, changes in the reflection spectrum are represented in decibel as $\Delta S(f,\, f_c)$, where f denotes frequency content of the signal with center frequency f_c, for DS04, DS03, DS02, and DS01 cylinders.
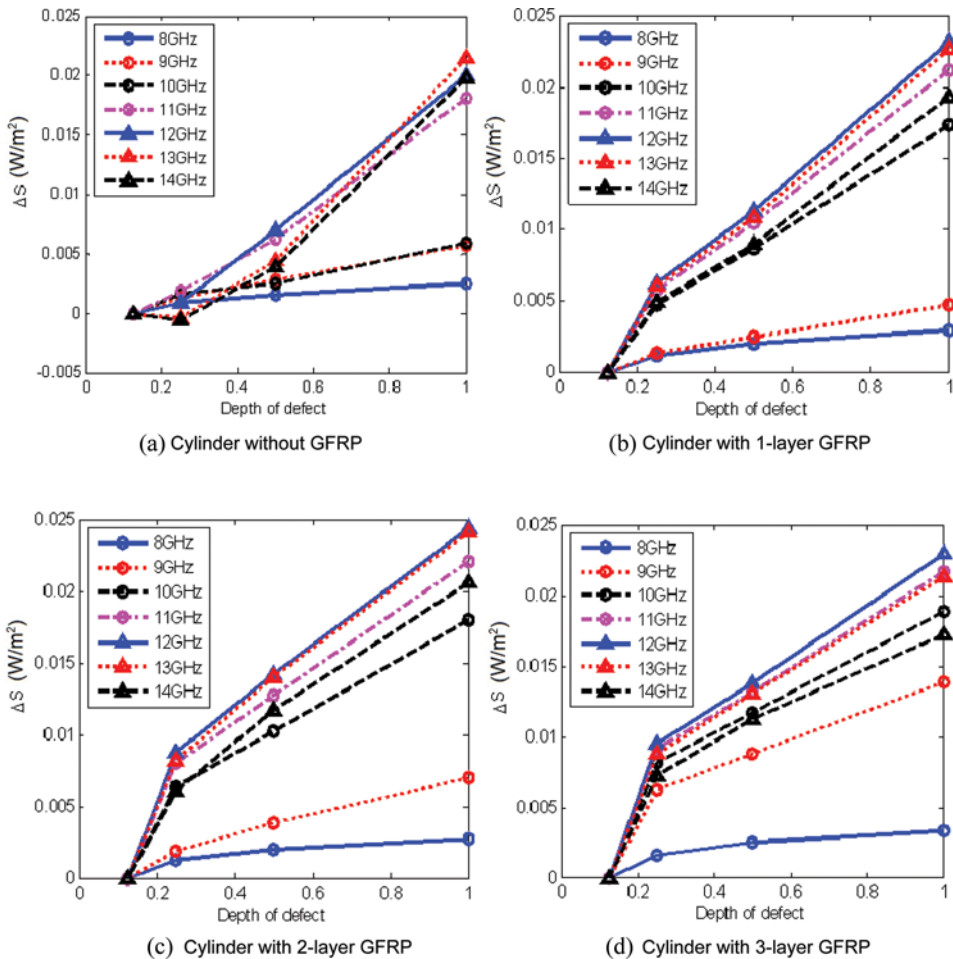

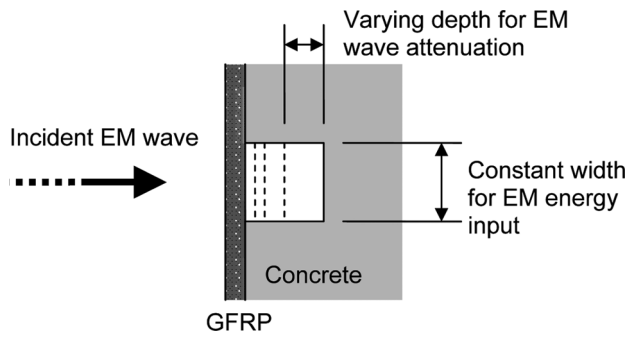FIGURE 18. Depth of defect vs. GFRP thickness. (Figure appears in color online.)

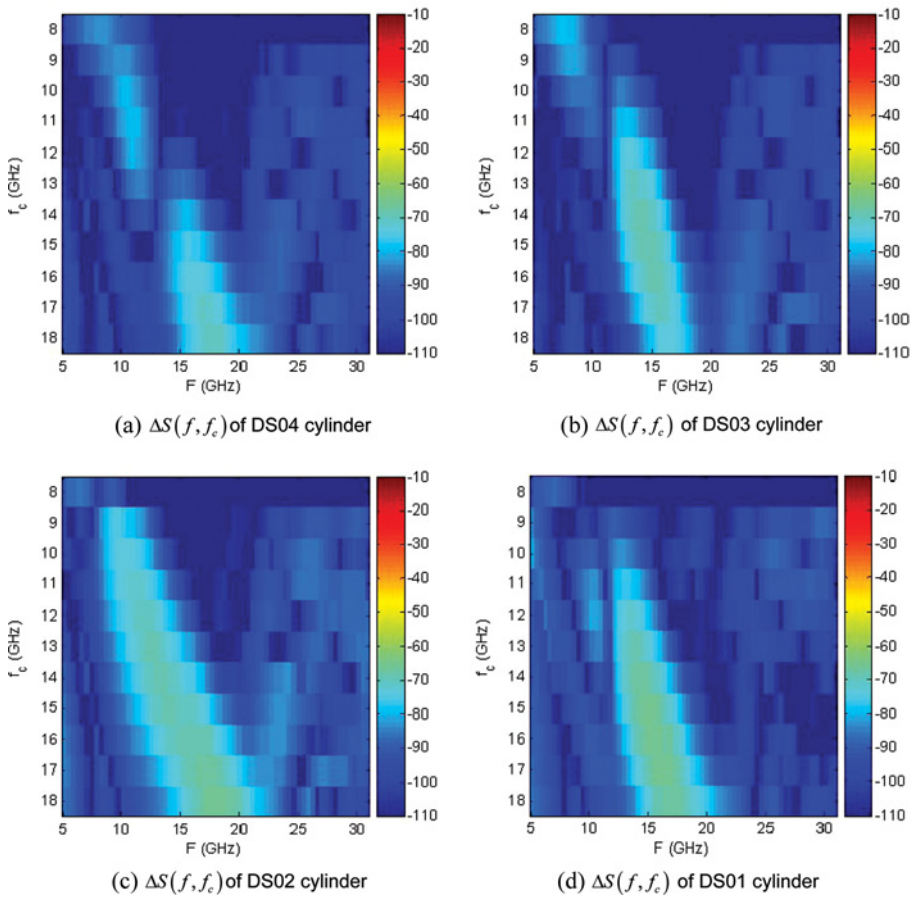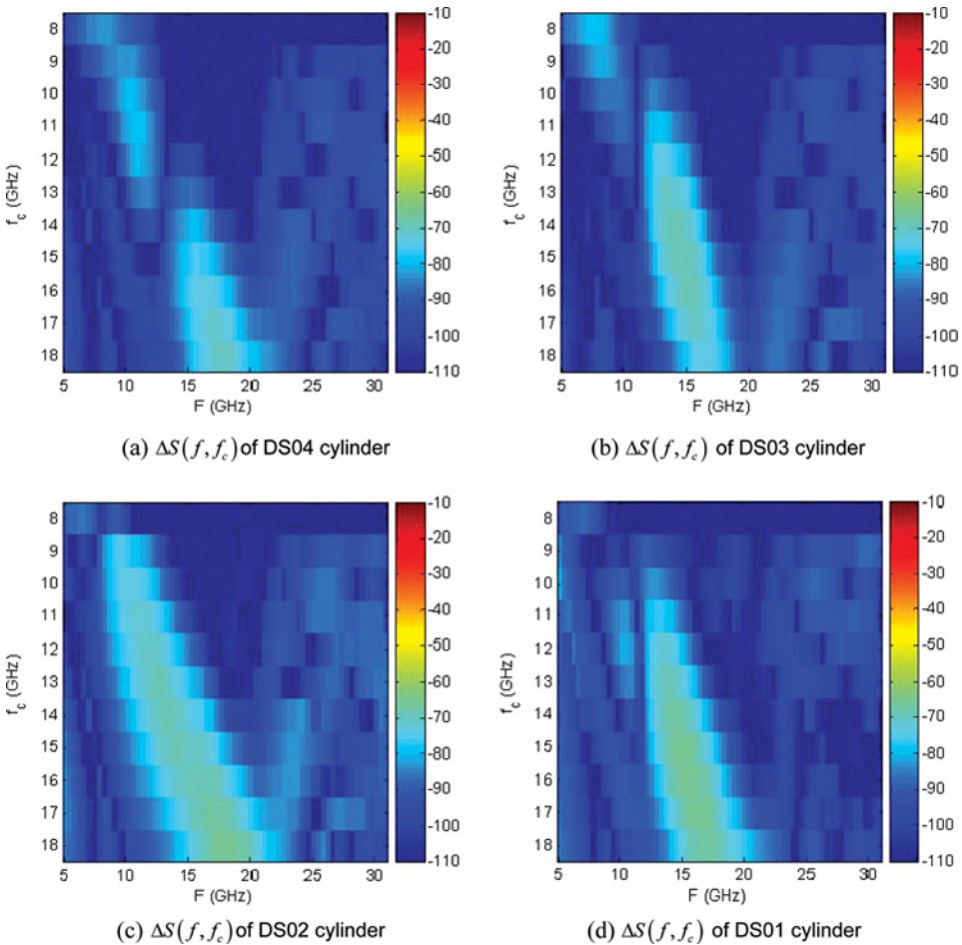**FIGURE 19.** A simplified model for explaining the effect of defect depth.

FIGURE 20. ΔS (f, f_c) of damaged cylinders. (Figure appears in color online.)

3.3. Effects of Defect Width

To study the effect of defect width in the reflection response of GFRP-concrete cylinders, responses of DS07 (width = 0.3175 cm or 1/8 in), DS06 (width = 0.635 cm or 1/4 in), DS05 (width = 1.27 cm or 1/2 in), and DS01 (width = 2.54 cm or 1 in) cylinders (Table 1) with 1-layer GFRP wrapping were compared. The defect depth was kept as 2.54 cm (1 in) for all cases. Figure 21 shows the amplitude of maximum reflection power response with respect to various defect widths and frequencies. The damaged cylinder with 2.54 cm (1 in) depth defect produces stronger reflection response than the ones of cylinders with 1/2-in, 1/4-in, 1/8-in, and 0-in defect depths,

FIGURE 21. Maximum power response of damaged cylinders with various defect widths and frequencies. (Figure appears in color online.)
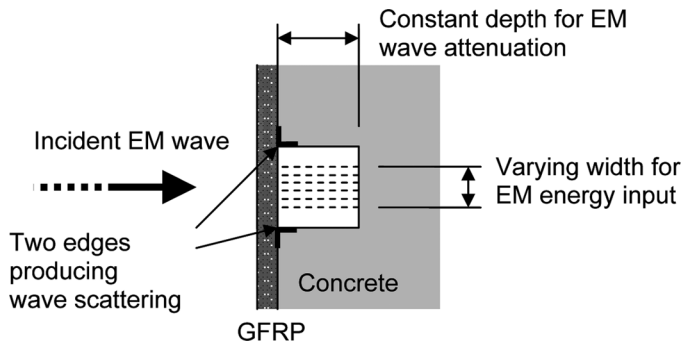
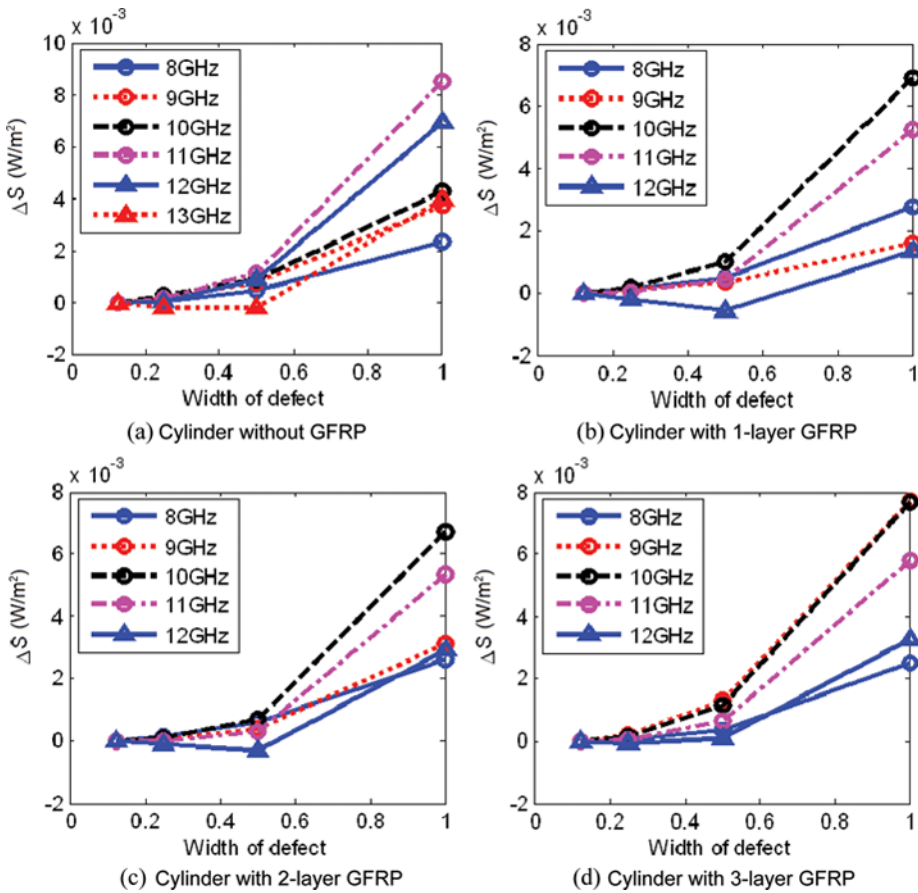**FIGURE 22.** A simplified model for explaining the effect of defect width.

FIGURE 23. Width of defect vs. GFRP thickness. (Figure appears in color online.)

as illustrated in Fig. 21(b), due to the difference in input energy. In addition, scattering from two edges of the defect also participated in the maximum reflection amplitude, as demonstrated in another simplified model shown in Fig. 22. Therefore, the defect width, edge scattering, and the incident carrier frequency jointly affected the maximum reflection power amplitude.

Comparison between intact and damaged cylinders, based on the difference in their maximum amplitudes, provides another observation on the effect of defect width. In Fig. 23(a), nonlinear increase of the maximum amplitude difference is found for cylinders with and without GFRP. Dramatic change of the difference occurs in certain frequencies when the defect width increases. In the considered simulation cases, EM waves of center/carrier frequencies from 8 GHz to 12 GHz exhibit such nonlinearity, corresponding

(a) $\Delta S(f, f_c)$ of DS07 cylinder

(b) $\Delta S(f, f_c)$ of DS06 cylinder

(c) $\Delta S(f, f_c)$ of DS05 cylinder

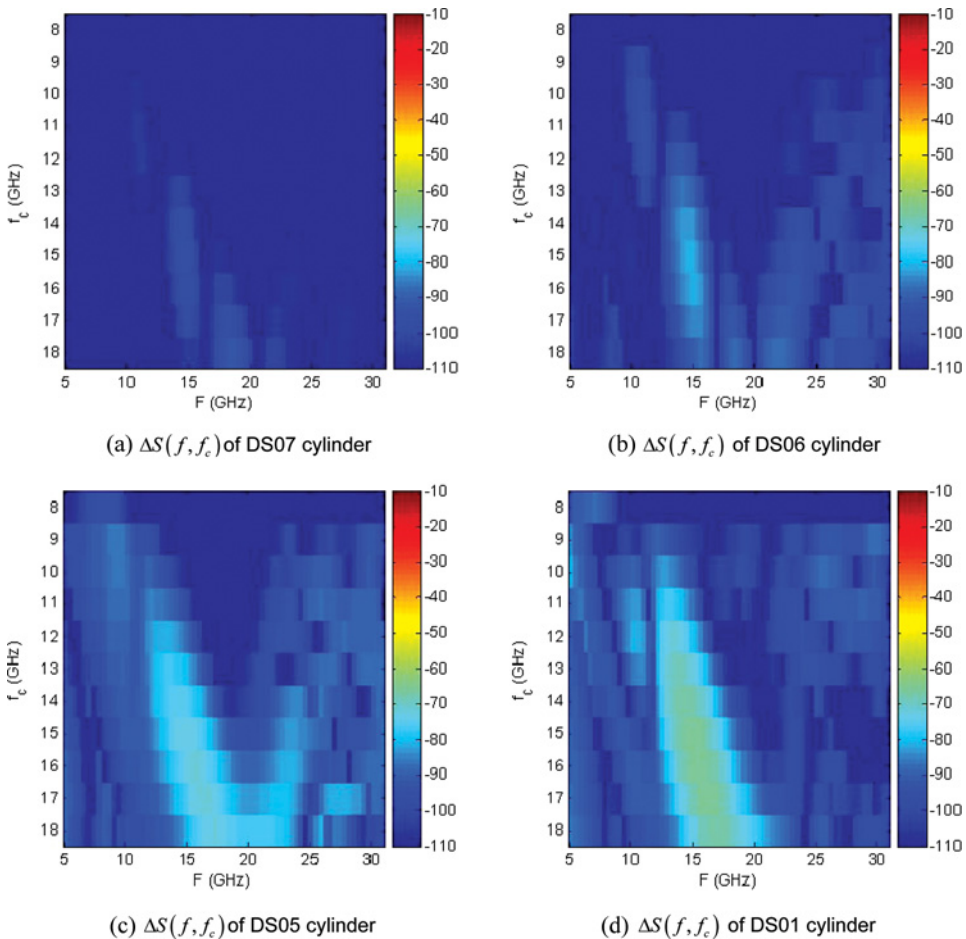(d) $\Delta S(f, f_c)$ of DS01 cylinder

FIGURE 24. $\Delta S(f, f_c)$ of damaged cylinders. (Figure appears in color online.)

to wavelengths of 0.0375–0.025 cm (1.47–0.98 in). The presence of GFRP seems to have a selective effect on incident frequency since the difference in maximum amplitude is sensitive to the presence of GFRP only in certain frequencies (9–11 GHz, in our study). Changes in the reflection spectrum are represented in decibel as $\Delta S(f, f_c)$, where f denotes frequency content of the signal with center frequency f_c, for DS07, DS06, DS05, and DS01 cylinders as shown in Fig. 24.

4. CONCLUSIONS

A parametric study for the transient reflection response of GFRP-wrapped concrete cylinders was conducted using the finite difference time domain simulation. GFRP-concrete cylinders with and without a subsurface artificial defect were considered. Simulation results showed that the increase of GFRP thickness encourages the scattering effect in both time and frequency responses of GFRP-concrete cylinders. Artificial defects with same volume but different aspect ratios produced different results in their responses. Simulation results are summarized as follows:

1. As expected, the presence of GFRP layer in the concrete cylinder provided extra delay in the time domain reflection response. The lossness of GFRP also introduced additional amplitude attenuation to the reflected waves when comparing with the one without GFRP.
2. Unlike the response of a planar stratified medium subjected to plane waves, creeping waves can occur on the circular surface of cylinders. The role of creeping waves in the maximum reflection amplitude are determined by two factors: i) the creeping waves propagating within the GFRP layer travel faster than the transmitting wave in the concrete cylinder due to the difference in their dielectric properties; and ii) the creeping waves in GFRP travel at a longer distance than the one of directly transmitting wave in concrete to reach the reflection line (Fig. 12) in order to interfere with the maximum reflection amplitude. As the combined result of these two factors, maximum amplitude of reflected waves not only varies with the GFRP thickness but also with the incident frequency.
3. Changes of waveform occur at frequencies where the intersection of curves was observed in the figures of maximum amplitude vs. center/carrier frequency (Fig. 15). This is due to the coupling of frequency change and increase of GFRP thickness.
4. In the power spectrum of reflection response from intact cylinders without GFRP, one main-lobe and one side-lobe were identified (Fig. 16(a)). With the presence of GFRP, additional frequency contents were introduced to the spectrum. The side-lobe becomes less distinguishable when the thickness of GFRP increases (Fig. 16).

5. For the effects of defect depth in reflection response, the damaged cylinder with 1-in defect depth generated stronger reflection response than the cylinders with defect of ½-in, ¼-in, ⅛-in, and 0-in depths (Fig. 17(b)). This difference is more significant in low frequencies (8–14 GHz).

6. Proportionality was observed in the maximum power density difference extracted from intact and damaged concrete cylinders with various depths (Fig. 18(a)). This behavior is changed by the introduction of GFRP layer (Fig. 18(b)–(d)). Increasing GFRP thickness enhances the proportionality between the maximum power density difference and the defect depth for GFRP-concrete cylinders.

7. A nonlinear effect in the maximum power density difference was found for cylinders with various defect widths. This is attributed to i) the difference in input EM energy into the defect, and ii) the scattering from two edges of the detect (Fig. 22). Increasing GFRP thickness also encourages low frequency (8–12 GHz) response to demonstrate such nonlinearity (Fig. 23).

8. Pattern development in frequency spectrum owing to the changes in defect depth and defect width was observed in Figs. 20 and 24, respectively. Gradual and regular development was found in the effects of defect width (Fig. 24). Such frequency-frequency response can be used for better understanding the nonlinear behaviors of reflected wave from circularly stratified lossy dielectric structures (e.g., GFRP-concrete cylinder) with one or many subsurface local scatterers (e.g., artificial defect, delamination, concrete cracking).

ACKNOWLEDGMENTS

REFERENCES

1. H. Saadatmanesh, M. R. Ehsani, and L. Jin. *ACI Structural Journal* **93**:639–647 (1996).
2. G. Steckel, G. Hawkins, and J. Bauer. *Proceedings of the 44th International SAMPE Symposium,* Long Beach, CA, pp. 2194–2208 (1999).
3. J. F. Bonacci and M. Maalej. *Journal of Infrastructure Systems, ASCE* **6**:41–51 (2000).
4. C. E. Bakis, L. C. Bank, V. L. Brown, E. Cosenza, J. F. Davalos, J. J. Lesko, A. Machida, S. H. Rikalla, and T. C. Triantafillou. *Journal of Composites for Construction, ASCE* **6**:73–87 (2002).
5. S. Rizkalla and A. Nanni. (eds.). *Field Applications of FRP Reinforcement: Case Study*, SP-215. ACI International. Farmington Hills, MI (2003).
6. H. Saadatmanesh and M. R. Ehsani. *Structural Materials.* J. Orofino (Ed.) (1989).
7. H. Saadatmanesh, M. Ehsani, and L. Jin. *ACI Structural Journal* **93**:639–647 (1996).
8. P. Mukhopadhyaya, N. Swamy, and C. Lynsdale. Optimizing structural response of beams strengthened with GFRP plates. *Journal of Composites for Construction, ASCE* **2**(**2, May**):87–95 (1998).

9. L. Lam and J. G. Teng. Strength of RC cantilever slabs bonded with GFRP strips. *Journal of Composites for Construction, ASCE* **5**(**4**), November:221–227 (2001).

10. S. Ross, A. Boyd, M. Johnson, R. Sexsmith, and N. Banthia. Potential retrofit methods for concrete channel beam bridges using glass fiber reinforced polymer. *Journal of Bridge Engineering, ASCE* **9**(**1**), January:66–74 (2004).

11. A. A. El Damatty, M. Abushagur, and M. A. Yousssef. Rehabilitation of composite steel bridges using GFRP plates. *Applied Composite Materials* **12**:309–325 (2005).

12. A. Mirmiran and S. Philip. Comparison of acoustic emission activity in steel-reinforced and FRP-reinforced concrete beams. *Construction and Building Materials* **14**:299–310 (2000).

13. G. Swit. Evaluation of compliance changes in concrete beams reinforced by glass fiber reinforced plastics using acoustic emission. *Journal of Materials in Civil Engineering, ASCE* **16**(**5**), October:414–418 (2004).

14. F. Bastianini, A. D. Tommaso, and G. Pascale. Ultrasonic non-destructive assessment of bonding defects in composite structural strengthenings. *Composite Structures* **53**:463–467 (2001).

15. A. Mirmiran and Y. Wei. Damage assessment of FRP-encased concrete using ultrasonic pulse velocity. *Journal Engineering Mechanics, ASCE* **127**(**2**):126–135 (2001).

16. J. R. Berriman, D. A. Hutchins, A. Neild, T. H. Gan, and P. Purnell. The application of time-frequency analysis to the air-coupled ultrasonic testing of concrete. *IEEE Transaction on Ultrasonics, Ferroelectrics, and Frequency Control* **53**(**4**), April:768–777 (2006).

17. M. A. Starnes, N. J. Carino, and E. Kausel. Preliminary thermography studied for quality control of concrete structures strengthened with fiber-reinforce polymer composites. *Journal of Materials in Civil Engineering, ASCE* **15**(**3**), June:266–273 (2003).

18. O. Hag-Elasfi, S. Alampalli, and J. Kunin. In-service evaluation of a reinforced concrete T-beam bridge FRP strengthening system. *Composite Structures* **64**:179–188 (2004).

19. R. D. Owen. Portable linear accelerators for X-ray and electro-beam applications in civil engineering. *NDT&E International* **31**(**6**):401–409 (1998).

20. O. Buyukozturk and H. C. Rhim. Electromagnetic Properties of Concrete for Nondestructive Testing,'' *Proceedings of the International Conference on Nondestructive Testing of Concrete in the Infrastructure*, Society for Experimental Mechanics, Deaborn, MI, pp. 83–92 (1993).

21. Ch. Maierhofer, M. Krause, and H. Wiggenhauser. Non-destructive investigation of sluices using radar and ultrasonic impulse echo. *NDT&E International* **31**(**6**):421–427 (1998).

22. M. Feng, F. D. Flaviis, and Y. J. Kim. Use of Microwaves for Damage Detection of Fiber Reinforced Polymer-Wrapped Concrete Structures. *Journal of Engineering Mechanics, ASCE* **128**(**2**):172–183 (2002).

23. J. A. Kong. *Electromagnetic Wave Theory*. EMW Publishing, Cambridge, MA (2000).

24. K. S. Yee. Numerical solution of initial boundary value problems involving Maxwell's equations in isotropic media. *IEEE Transactions on Antennas and Propagation* **AP-14**(**3**):302–307 (1966).

25. R. Courant, K. Friedrichs, and H. Lewy. On the partial difference equations of mathematical physics. *IBM Journal of Research and Development* **11**(**2**):215–234 (1967).

26. A. Taflove and M. E. Brodwin. Numerical solution of steady-state electromagnetic scattering problems using the time-dependent Maxwell's equations. *IEEE Transactions on Microwave Theory and Techniques* **MTT-23**(**8**):623–630 (1975).

27. J.-P. Berenger. A perfectly matched layer for the absorption of electromagnetic waves. *Journal of Computational Physics* **114**(**2**):185–200 (1994).

28. J.-P. Berenger. Perfectly matched layer for the FDTD solution of wave-structure interaction problems. *IEEE Transactions on Antennas and Propagation* **44**(**1**), January:110–117 (1996).

29. J.-P. Berenger. Improved PML for the FDTD solution of wave-structure interaction problems. *IEEE Transactions on Antennas and Propagation* **45**(**3**), March:466–473 (1997).

30. H. C. Rhim and O. Buyukozturk. Wideband microwave imaging of concrete for nondestructive testing. *ASCE Journal of Structural Engineering* **126**(**12**):1451–1457 (2000).